

## A novel compensation method for the anode gain non-uniformity of multi-anode photomultiplier tubes

Chan Mi Lee<sup>1,2,3</sup>, Sun Il Kwon<sup>1,3,4</sup>, Guen Bae Ko<sup>1,2,3</sup>, Mikiko Ito<sup>1,3</sup>,  
Hyun Suk Yoon<sup>1,2</sup>, Dong Soo Lee<sup>1,3,4,5</sup>, Seong Jong Hong<sup>6</sup>  
and Jae Sung Lee<sup>1,2,3,4,7,8</sup>

<sup>1</sup> Department of Medicine, Seoul National University, Seoul, Korea

<sup>2</sup> Department of Biomedical Sciences, Seoul National University, Seoul, Korea

<sup>3</sup> Institute of Radiation Medicine, Medical Research Center, Seoul National University, Seoul, Korea

<sup>4</sup> Interdisciplinary Program in Radiation Applied Life Science, Seoul National University, Seoul, Korea

<sup>5</sup> Department of Molecular Medicine and Biopharmaceutical Sciences, Seoul National University, Seoul, Korea

<sup>6</sup> Department of Radiological Science, Eulji University, Gyeonggi-do, Korea

<sup>7</sup> Department of Brain and Cognitive Sciences, Seoul National University, Seoul, Korea

E-mail: [jaes@snu.ac.kr](mailto:jaes@snu.ac.kr)

Received 16 May 2011, in final form 8 November 2011

Published 7 December 2011

Online at [stacks.iop.org/PMB/57/191](http://stacks.iop.org/PMB/57/191)

### Abstract

The position-sensitive multi-anode photomultiplier tube (MA-PMT) is widely used in high-resolution scintillation detectors. However, the anode gain non-uniformity of this device is a limiting factor that degrades the intrinsic performance of the detector module. The aim of this work was to develop a gain compensation method for the MA-PMT and evaluate the resulting enhancement in the performance of the detector. The method employs a circuit that is composed only of resistors and is placed between the MA-PMT and a resistive charge division network (RCN) used for position encoding. The goal of the circuit is to divide the output current from each anode, so the same current flows into the RCN regardless of the anode gain. The current division is controlled by the combination of a fixed-value series resistor with an output impedance that is much larger than the input impedance of the RCN, and a parallel resistor, which detours part of the current to ground. PSpice simulations of the compensation circuit and the RCN were performed to determine optimal values for the compensation resistors when used with Hamamatsu H8500 MA-PMTs. The intrinsic characteristics of a detector module consisting of this MA-PMT and a lutetium-gadolinium-oxyorthosilicate (LGSO) crystal array were tested with and without the gain compensation method. In simulation, the average coefficient of variation and max/min ratio decreased from 15.7% to 2.7% and 2.0 to 1.2, respectively. In the flood map of the LGSO-H8500

<sup>8</sup> Author to whom any correspondence should be addressed.

detector, the uniformity of the photopeak position for individual crystals and the energy resolution were much improved. The feasibility of the method was shown by applying it to an octagonal prototype positron emission tomography scanner.

(Some figures may appear in colour only in the online journal)

## 1. Introduction

Nuclear medicine (NM) imaging devices, such as single photon emission computed tomography (SPECT) and positron emission tomography (PET) scanners, are widely used for the diagnosis and treatment monitoring of a variety of diseases (Zhu and Shim 2011, Lee *et al* 2011). NM imaging devices provide image data that visualize the distribution of radiopharmaceuticals within living bodies. Many devices dedicated to imaging small animals or specific human organs have been developed. Such devices require high spatial resolution and gamma-ray detection sensitivity (Pichler *et al* 2008, Lee 2010), and increasingly make use of the position-sensitive multi-anode photomultiplier tubes (MA-PMTs). PSPMTs are compact, and have a wide effective area and an excellent intrinsic resolution, because of the integration of tens to hundreds of anodes (Rouze *et al* 2004, Olcott *et al* 2005, More *et al* 2006, Loudos *et al* 2007, Pani *et al* 2007, Hong *et al* 2008, Raylman *et al* 2008, Alva-Sanchez *et al* 2010, Ito *et al* 2010a, 2010b). A position-sensitive MA-PMT can be used together with an array of tiny scintillation crystals to yield a scintillation detector with high intrinsic spatial resolution.

However, MA-PMTs have a non-uniform anode gain, which can degrade the intrinsic performance of MA-PMT-based detector modules. In particular, the gain non-uniformity distorts the event position and signal amplitude linearity, and reduces the effective dynamic range of the readout (Popov and Majewski 2006, Popov *et al* 2006). Moreover, the dead-time loss in scintillation detector modules occurs because the MA-PMT output signal requires a relatively low trigger level. Previous approaches to overcome these limitations have different advantages and disadvantages, as will be described in section 4.

In this work, we devised an alternative method for performing gain compensation on the MA-PMT. This method is based on a 2D resistive charge division network (RCN), which is a discrete version of a single-wire, position-sensitive proportional counter readout (Siegel *et al* 1996). We describe the simulation and experimental studies we performed to investigate the feasibility of the proposed method, and show an example PET scanner to which the method was applied.

## 2. Materials and methods

### 2.1. Position-sensitive MA-PMT

A Hamamatsu H8500 MA-PMT was used to study our gain compensation method. The H8500 MA-PMT has 64 output channels in a square  $8 \times 8$  arrangement. It is useful in high performance, small field of view (FOV) imaging systems because of its compact anode size ( $5.8 \times 5.8 \text{ mm}^2$ ), which is assembled with a very narrow inter-anode spacing (0.28 mm).

Figure 1 shows the anode gain uniformity distribution of a typical H8500, as provided by the manufacturer. These values were obtained for each channel using a tungsten lamp with a

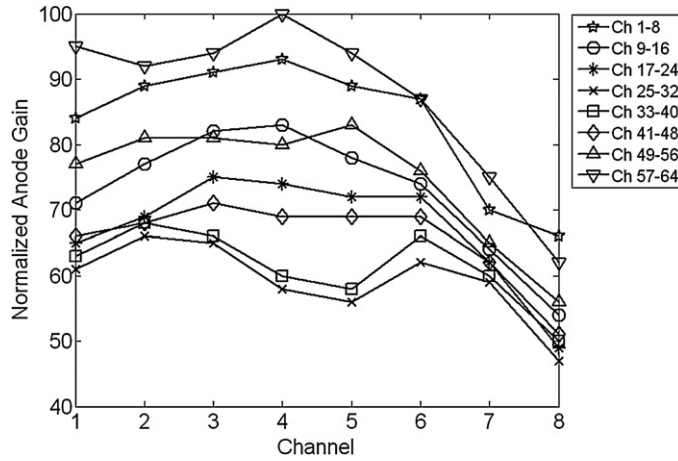


**Figure 1.** Normalized anode gain distribution map of a typical position-sensitive MA-PMT (H8500, Hamamatsu Photonics), as provided by the manufacturer. The mean  $\pm$  standard deviation is  $71.5 \pm 12.7$  and the COV is 17.8%.

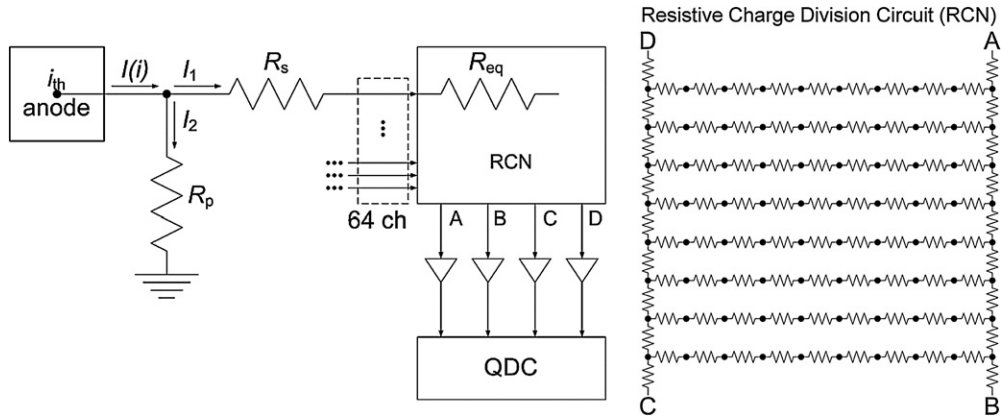


**Figure 2.** Schematic of the proposed gain compensation method. The goal of the circuit is to make the same amount of current ( $I_1$ ) flow from each anode into the RCN.

blue filter running at a supply voltage of  $-1000$  V. We see that the gain varies by up to 2:1, depending on the channel.

## 2.2. Gain compensation method

Figure 2 outlines the gain compensation method devised in this work. The anode signal from the MA-PMT is treated as a current source. The output current from each anode,  $I(i)$ , is divided so that the current flowing into the corresponding anode of the RCN,  $I_1$ , is the same for all anodes. The circuit is designed to make the magnitude of  $I_1$  equal to the current from the anode with minimum output gain,  $I_{\min}$ . The remaining current from the  $i$ th anode ( $I_2 = I(i) - I_{\min}$ ) flows to the ground.

The gain compensation method for a 2D RCN is implemented by applying a parallel resistor,  $R_p$ , and a series resistor,  $R_s$ , to each channel. The division of the current is controlled

by the ratio of  $R_p$  to  $R_s$ , as shown in the following equation, where it is assumed that the input impedance of the RCN,  $R_{eq}$ , is negligibly small relative to  $R_s$ :

$$I_2 = \frac{R_s}{R_p(i)} I_1. \quad (1)$$

Thus,  $R_s$  is fixed at a value much larger than  $R_{eq}$ , and  $R_p$  is varied to compensate for each MA-PMT channel. The value of  $R_p(i)$  for the  $i$ th channel is determined with the equation below:

$$R_p(i) = \frac{I_1}{I_2} R_s = \frac{I_{\min}}{I(i) - I_{\min}} R_s. \quad (2)$$

### 2.3. Simulation study for concept verification

The feasibility of our method was examined using the PSpice simulation toolkit (OrCAD 10.5), a circuit simulator. The circuits for the gain compensation, RCN and amplifier units were included in the simulation. Each current source input to the gain compensation circuit was simulated as a sinusoidal function with a magnitude,  $I(i)$ , proportional to the gain distribution shown in figure 1. The output signals from the compensation circuit were multiplexed in the RCN to produce four weighted-sum signals ( $A$ ,  $B$ ,  $C$  and  $D$ ), which were amplified by charge-sensitive amplifiers. Because the sum of the RCN outputs ( $S = A + B + C + D$ ) is proportional to  $I_1$  (the compensated anode output), the performance of the gain compensation was evaluated by activating a single anode and assessing the uniformity of the distribution of  $S$ .

### 2.4. Block detector design

In addition to our simulations, the performance of our gain compensation method was evaluated using real detector modules consisting of an H8500 MA-PMT and a crystal array. The crystal array consists of a  $29 \times 29$  polished lutetium gadolinium oxyorthosilicate ( $\text{Lu}_{1.8}\text{Gd}_{0.2}\text{SiO}_4$ : Ce, LGSO) scintillator (dimensions:  $1.5 \times 1.5 \times 7 \text{ mm}^3$ ; crystal pitch: 1.65 mm), which showed excellent characteristics in the development of high-resolution PET detectors in our previous studies (Hong *et al* 2008, Kwon *et al* 2011). The crystal arrays were assembled using reflector grids composed of 3M enhanced spectral reflector polymer (thickness: 0.065 mm). Optical grease (Saint-Gobain, BC-630, index of refraction: 1.465) was used to optically couple the crystal array to the MA-PMT.

The readout electronics (the gain compensation, RCN and amplifier circuits) were also constructed, as shown in figure 3, where they are connected to the H8500 MA-PMT (1). The correction resistors,  $R_s$  and  $R_p$ , for each channel are surface mounted on the gain compensation boards (2). The RCN board (3) processes the 64 outputs from the gain compensation boards. The amplifier board (4) processes the four outputs from the RCN board, and the dynode output signal from the H8500, which is used for event triggering. Because resistors with the exact  $R_p$  values determined in the PSpice simulation were unavailable, two resistors were combined in series to obtain a close approximation. The resulting average error between the exact and approximate  $R_p$  values was less than 1%.

### 2.5. Experimental details

Figure 4 shows a schematic of the test setup used to obtain the pulse height spectra and flood maps of the detector modules. The front side of each detector module was irradiated with a 1.25 MBq  $^{22}\text{Na}$  point source with a nominal diameter of 0.25 mm. Coincidence

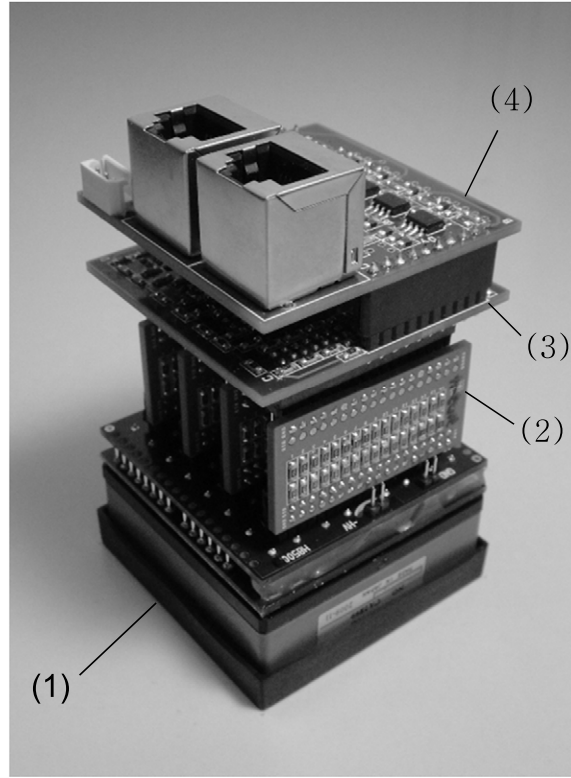


**Figure 3.** A H8500 MA-PMT (1) connected to the readout electronics, which include the gain compensation circuits (2), the position encoding RCN (3), and the charge-sensitive amplifier units (4).

data were acquired with a coincidence detector, which consists of an H8500 MA-PMT and a  $7 \times 7$  LGSO ( $[\text{Lu}_{1.8}\text{Gd}_{0.2}\text{SiO}_4:\text{Ce}]$ ; Hitachi Chemical Co., Ltd) scintillator array (dimensions:  $1.5 \times 1.5 \times 7.0 \text{ mm}^3$ ; crystal pitch: 1.65 mm). The distance between the test detector and the coincidence detector was 25 cm. The detector modules were tested with and without gain compensation.

The dynode outputs from the detector modules were used to generate coincidence signals, which were input to nuclear instrumentation module and VME (Versa Module Eurocard) modules to initiate the measurement of energy and position. Appropriate cable lengths were added to ensure that signals arrived within the gate period of the charge-to-digital converter (QDC). We used a constant fraction discrimination (CFD) module (KN381, CAEN) to discriminate signals from noise, and coincidence logic (N455, CAEN) to determine coincident events from the CFD outputs. Finally, a QDC VME module (V965, CAEN) was used to measure the integrated charges.

Flood maps were generated from the detector modules by decoding the gamma-ray interaction position ( $X, Y$ ) from the  $A, B, C$  and  $D$  signals, as given by the following equations:

$$X = \frac{(A + B) - (C + D)}{S}, \quad Y = \frac{(A + D) - (B + C)}{S}, \quad S = A + B + C + D. \quad (3)$$

The crystal map was generated from the flood map automatically by searching for local peaks in the flood map and calculating the minimum distance between the peaks

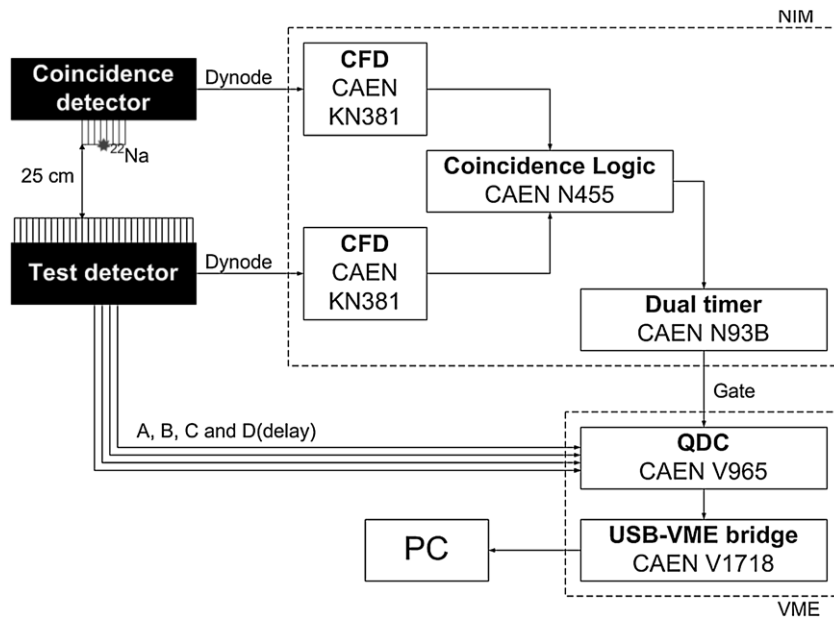


**Figure 4.** Schematic diagram of the test setup used to obtain the pulse height spectra and flood maps of the detector modules.

(Kwon *et al* 2008). The uniformity of the photopeak position in the energy spectrum of each crystal was then evaluated.

### 2.6. Prototype PET scanner

The gain-compensated detector modules developed in this work were applied to a prototype, small-ring PET scanner with eight detector modules. The scanner was designed for imaging small animals, such as rats and mice. The face-to-face distance between two opposite detectors was 13.1 cm. A detailed description of the PET scanner is given in table 1. The four position signals from each detector module were digitized (sampling rate = 170 MHz) and processed using the field-programmable gate array (FPGA)-based acquisition boards, in which the digital baseline correction and energy calculation are carried out. The events determined as valid in the acquisition boards were transferred to a master board that is also based on FPGA (Virtex 5; Xilinx). Here, the coincidence events between all the combinations of detector pairs were determined and sent to a main computer through Gigabit Ethernet (Ko *et al* 2011). The coincidence window of 12 ns was used.

To measure spatial resolution and sensitivity, we used the  $^{22}\text{Na}$  point source with nominal diameter of 250  $\mu\text{m}$  (activity = 1.11 MBq; Isotope Products Laboratories) embedded with an acrylic disc.

For the measurement of spatial resolution at various positions, the point source was positioned at the center of the PET scanner and moved in the radial direction to 30 mm with 2 mm step size. At each location, list-mode PET data were acquired for 5 min with the energy window of 400–600 keV. The list-mode data were sorted into a three-dimensional sinogram and then rebinned into two-dimensional data using the single-slice rebinning algorithm. Finally, the PET data were reconstructed using the maximum-likelihood expectation-maximization

**Table 1.** Major characteristics of prototype PET scanner.

Characteristics	Value
Crystal	L <sub>0.9</sub> GSO
Size (mm <sup>3</sup> )	1.5 × 1.5 × 7.0
Pitch (mm)	1.65
No/block	841 (29 × 29)
PMT	H8500
No of channels	64 (8 × 8)
Anode size (mm <sup>2</sup> )	5.8 × 5.8
PET scanner	
No of detector blocks	8
No of crystal rings	29
Ring diameter (cm)	13.1
Axial FOV (cm)	4.8

L<sub>0.9</sub>GSO: Lu<sub>1.8</sub>Gd<sub>0.2</sub>SiO<sub>4</sub>:Ce.

PMT: photomultiplier tube.

PET: positron emission tomography.

FOV: field of view.

(MLEM) algorithm (iteration number = 16). We used the MLEM algorithm because the gaps between H8500 PMTs led to significant reconstruction artifacts when a filtered back-projection reconstruction algorithm was applied. The spatial resolution was measured as the full-width at half-maximum (FWHM), which was estimated using linear interpolation (National Electrical Manufacturers Association 2008, Kim *et al* 2007, Kwon *et al* 2011).

To measure the sensitivity, the <sup>22</sup>Na point source placed at the transaxial center was moved to the axial range of −23–23 mm and scanned for 5 min at each axial position. The activity of the point source was corrected for the branching ratio. Three different energy windows were applied (250–750, 350–650 and 400–600 keV).

To show the feasibility of the scanner for small-animal imaging, PET studies were performed on a rat. The rat was anesthetized by the continuous administration of isoflurane in oxygen. A 30 min PET scan of a Sprague Dawley rat (240 g) brain was acquired for 50 min after the injection of [<sup>18</sup>F]FDG 47.5 MBq. PET data were processed using the same procedures as used in the spatial resolution measurement.

The animal bed of the PET scanner was moved after the PET scan into the x-ray computed tomography (CT) gantry to acquire the CT image without the movement of the rat. We used small animal dedicated CT in the eXplore VISTA PET/CT scanner (GE Healthcare). The 360 projection data with 0.25 mA and 40 kV protocol were acquired (exposure time for each projection: 250 ms × 4 shots), and reconstructed into the 526 × 26 × 380 matrix (voxel size = 0.123 × 0.123 × 0.123 mm<sup>3</sup>).

A <sup>68</sup>Ge annulus phantom was scanned for 8 h to obtain the data for normalization correction that was applied to the phantom and animal data prior to the image reconstruction.

### 3. Results

#### 3.1. Simulation results

As described, the performance of the gain compensation method was evaluated in simulation by assessing the normalized distribution of the sum of the RCN output signals (the distribution of  $S$ ). Figure 5(a) shows the distribution of the normalized  $S$  after applying the primary gain compensation method defined by equation (2) to the MA-PMT with the distribution of

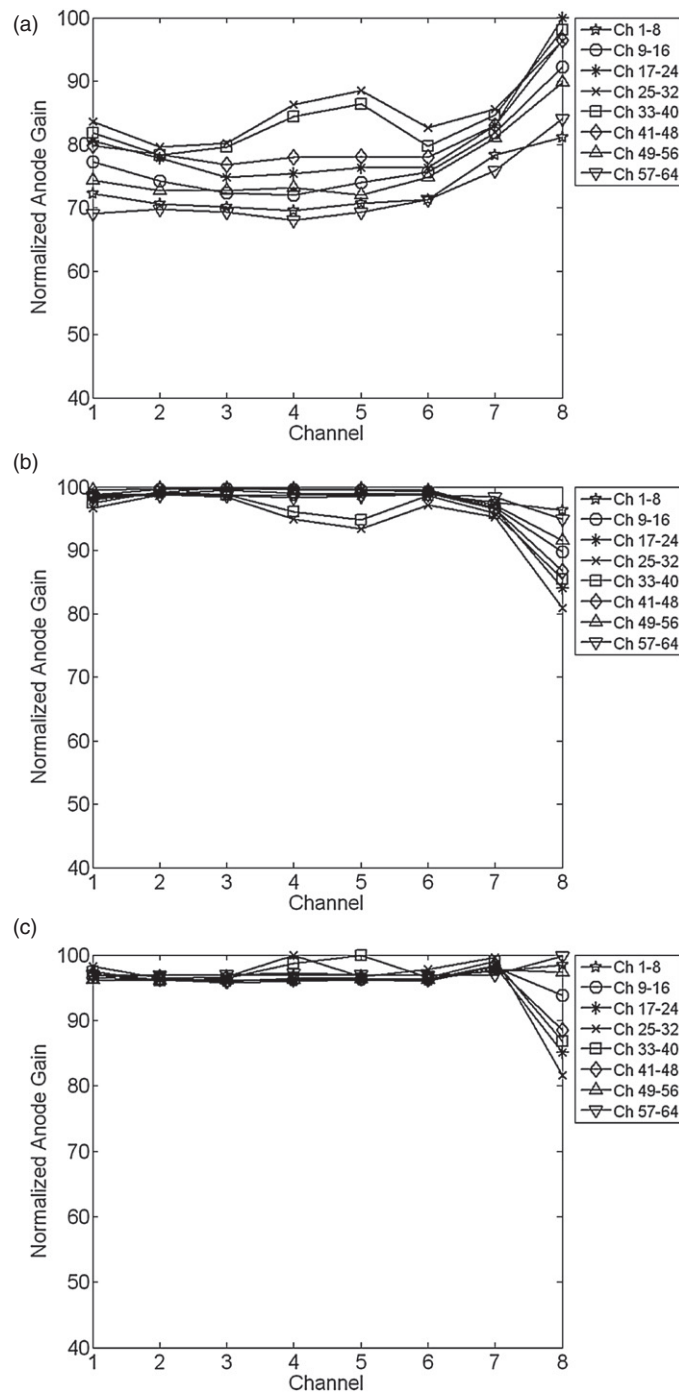


**Figure 5.** Distribution of the normalized RCN output signal (distribution of  $S$ ) after primary (a), secondary (b) and tertiary (c) compensations.

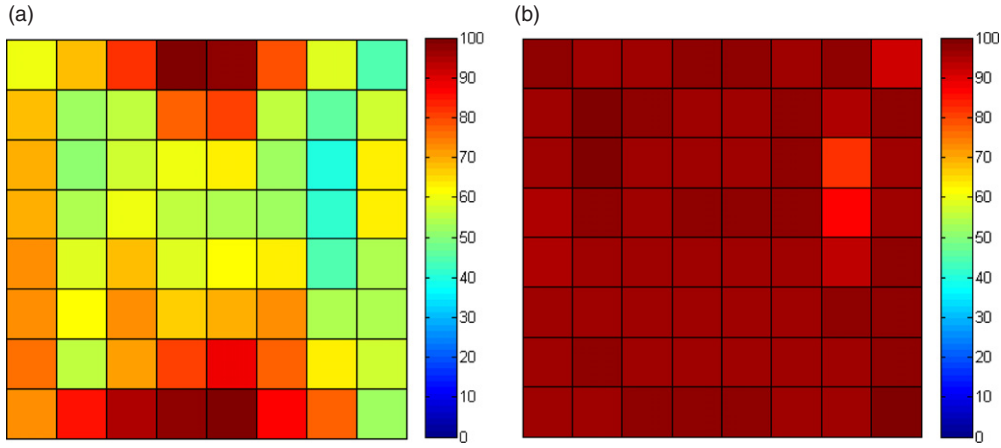


**Figure 6.** 2D distribution of  $S$  before (a) and after (b) gain compensation in a typical H8500 MA-PMT (COV decreased from 22.0% to 2.6%; max/min ratio decreased from 2.5 to 1.2).

figure 1. The compensated distribution shows that the output was not very uniform. To improve the uniformity, secondary and tertiary compensations were performed on the results of the primary compensation.

In the secondary compensation, the new parallel resistor values,  $R_{p2}(i)$ , were determined by

$$R_{p2}(i) = \frac{\alpha_1(i) \times I_{\min}}{I(i) - \alpha_1(i) \times I_{\min}} R_s, \quad (4a)$$

$$\alpha_1(i) = \frac{\max(S_1(i); i = 1, \dots, 64)}{S_1(i)}, \quad (4b)$$

where  $S_1(i)$  is the sum of the RCN outputs after primary compensation when  $I(i)$  was the output from the  $i$ th anode, and  $\max(S_1(i); i = 1, \dots, 64)$  is the maximum of the values of  $S_1(i)$ .

In the tertiary compensation, the new parallel resistor values,  $R_{p3}(i)$ , were determined by

$$R_{p3}(i) = \frac{\alpha_1(i) \times \alpha_2(i) \times I_{\min}}{I(i) - \alpha_1(i) \times \alpha_2(i) \times I_{\min}} R_s, \quad (5a)$$

$$\alpha_2(i) = \frac{\max(S_2(i); i = 1, \dots, 64)}{S_2(i)}, \quad (5b)$$

where  $S_2(i)$  is the sum of the RCN outputs after secondary compensation, and  $\max(S_2(i); i = 1, \dots, 64)$  is the maximum of the values of  $S_2(i)$ .

Figures 5(b) and (c) show the distribution of  $S$  after performing the secondary and tertiary compensations, respectively. These results indicate that the iterative application of gain compensation improved uniformity significantly. Figure 6 shows the 2D distribution of  $S$  before and after gain compensation in another H8500 MA-PMT. Here, the coefficient of variation (COV) of the normalized output and the ratio of the maximum to the minimum photopeak position (max/min ratio) were improved from 22.0% to 2.6% and 2.5 to 1.2, respectively.

Table 2 gives the simulated intrinsic uniformity results for 11 H8500 MA-PMTs. On average, the COV of the normalized output and the max/min ratio were improved from 15.7% to 2.7% and 2.0 to 1.2, respectively.

**Table 2.** The gain compensation simulation results for eleven H8500 MA-PMTs. The entries give the intrinsic uniformity of the MA-PMTs and the normalized sum of signals ( $S$ ) after primary, secondary and tertiary simulations (mean  $\pm$  standard deviation (COV)).

MA-PMT number	Intrinsic uniformity	Primary result	Secondary result	Tertiary result
1	82.7 $\pm$ 7.4 (9.0%)	92.4 $\pm$ 3.8 (4.1%)	96.6 $\pm$ 2.4 (2.5%)	96.8 $\pm$ 1.3 (1.3%)
2	80.3 $\pm$ 9.1 (11.3%)	86.8 $\pm$ 6.3 (7.3%)	94.1 $\pm$ 4.2 (4.5%)	95.3 $\pm$ 2.9 (3.0%)
3	70.5 $\pm$ 8.8 (12.5%)	86.8 $\pm$ 6.5 (7.5%)	91.0 $\pm$ 4.5 (4.9%)	95.6 $\pm$ 2.9 (3.0%)
4	68.9 $\pm$ 8.7 (12.6%)	83.8 $\pm$ 5.1 (6.1%)	95.6 $\pm$ 2.8 (2.9%)	96.2 $\pm$ 2.3 (2.4%)
5	74.6 $\pm$ 11.0 (14.7%)	82.1 $\pm$ 6.3 (7.7%)	96.5 $\pm$ 3.2 (3.3%)	96.0 $\pm$ 2.5 (2.6%)
6	72.9 $\pm$ 12.5 (17.1%)	80.8 $\pm$ 8.0 (9.9%)	96.1 $\pm$ 4.5 (4.7%)	94.3 $\pm$ 2.8 (3.0%)
7	71.0 $\pm$ 12.3 (17.3%)	85.0 $\pm$ 8.0 (9.4%)	94.6 $\pm$ 4.1 (4.3%)	95.0 $\pm$ 2.8 (2.9%)
8	71.5 $\pm$ 12.7 (17.8%)	78.7 $\pm$ 7.5 (9.5%)	97.1 $\pm$ 3.9 (4.0%)	96.3 $\pm$ 3.1 (3.2%)
9	70.6 $\pm$ 13.1 (18.6%)	73.6 $\pm$ 7.0 (9.5%)	97.7 $\pm$ 3.5 (3.6%)	94.0 $\pm$ 2.8 (3.0%)
10	68.5 $\pm$ 13.4 (19.6%)	81.0 $\pm$ 7.5 (9.3%)	96.7 $\pm$ 3.8 (3.9%)	95.4 $\pm$ 2.8 (2.9%)
11	66.0 $\pm$ 14.5 (22.0%)	77.4 $\pm$ 7.9 (10.2%)	96.9 $\pm$ 3.5 (3.6%)	96.1 $\pm$ 2.5 (2.6%)

### 3.2. Performance evaluation of block detectors

Figures 7–10 show the experimental results obtained using the block detector described in section 2.4 with and without gain compensation. Figure 7 shows the pulse height spectra of an H8500 block detector without (a) and with (b) gain compensation. Spectrum peak alignment to correct for the light output difference was not applied to individual crystals. The gain compensation yielded better discrimination of photopeak and scatter regions in the pulse height spectrum. The FWHM of the primary peak region was improved from 37.7% to 25.6%.

Figure 8 is the intrinsic uniformity map of a typical H8500 MA-PMT. Figures 9 and 10 show (a) flood images, (b) maps of the photopeak position in the energy spectrum of each element in the crystal array, (c) peak-aligned energy spectrum, (d) maps for energy resolution which were measured with the detector block using a PMT shown in figure 8 before (figure 9) and after (figure 10) gain compensation.

The flood images in figures 9(a) and 10(a) were generated by applying  $\pm 20\%$  energy windows to the raw pulse height spectra, and the serious non-uniform intensity distribution in the flood image was yielded without gain compensation as shown in figure 9(a). The distribution of photopeak position obtained without gain compensation (figure 9(b)) shows a similar pattern to the MA-PMT intrinsic uniformity shown in figure 8. In contrast, the gain compensation gave much better uniformity in the flood image and photopeak position (figures 10(a) and (b)).

Absolute photopeak values decreased after gain compensation because part of the current was diverted to the ground (figure 9(b) versus figure 10(b)). However, the decrease in the photopeak did not lead to any degradation in the image quality of the flood image, shape of the peak-aligned energy spectrum and energy resolution for each individual crystal as shown in figures 10(a), (c) and (d).

### 3.3. Prototype PET scanner

Figure 11 shows the prototype octagonal PET scanner (a) and eight detector modules (b) assembled in the scanner. The best and worst energy resolutions at 511 keV for all crystals were 11.3% and 69.8%, respectively. The energy resolutions, averaged over all detectors and crystals, were  $14.2\% \pm 3.0\%$ , respectively.

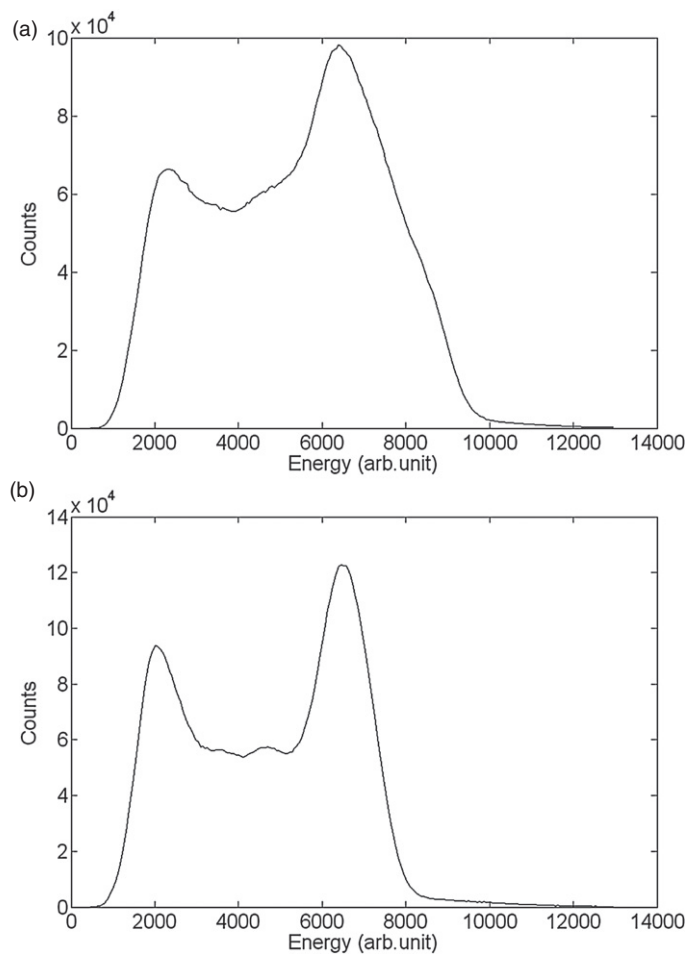
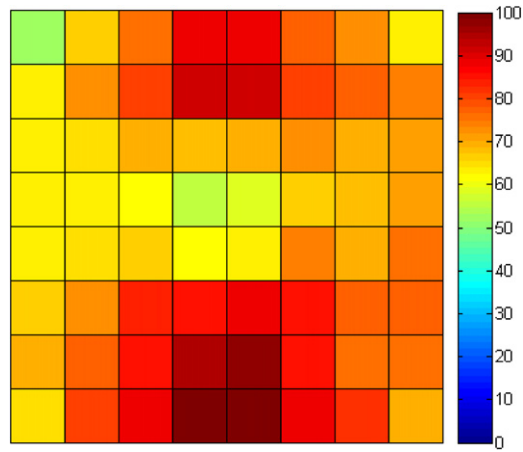


**Figure 7.** Pulse height spectra of a block detector before (a) and after (b) gain compensation (without peak alignment of the spectra for individual crystals).

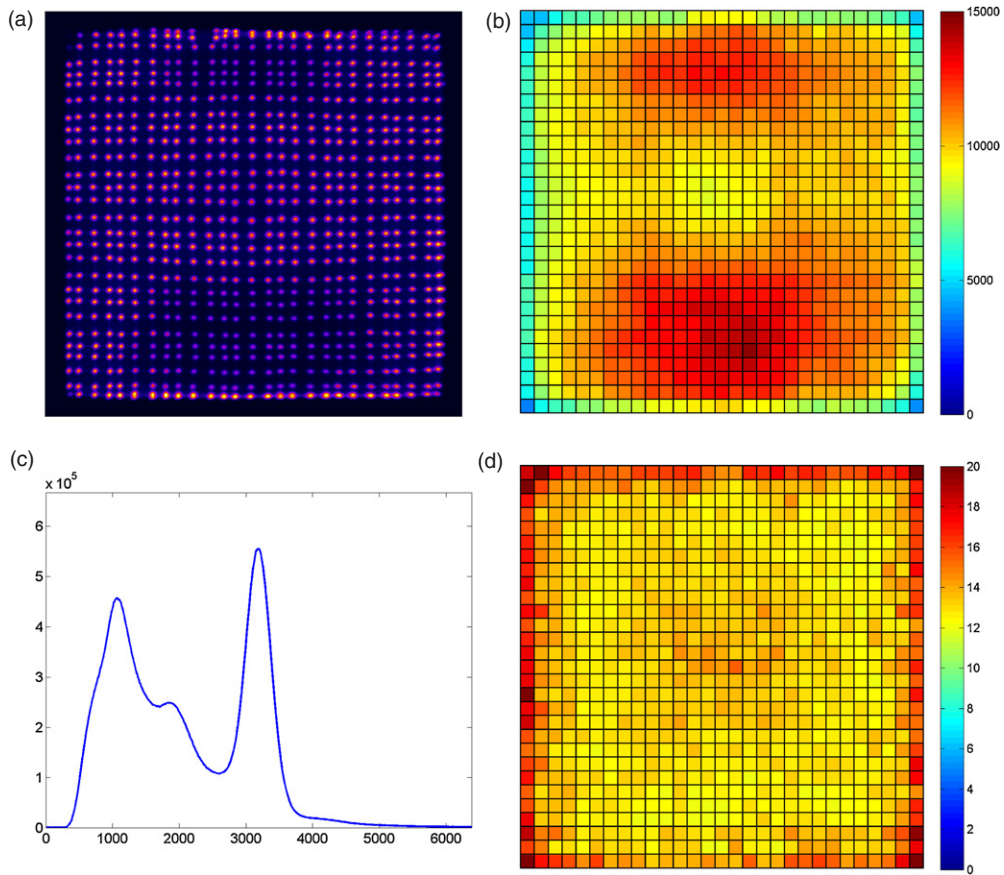
In figure 12, radial and tangential spatial resolutions acquired from the reconstructed images of the  $^{22}\text{Na}$  point source are plotted versus the radial offset from the center. Spatial resolution at the center was approximately 1.0 mm in both the radial and tangential directions. Although degradation in the spatial resolution was observed at the periphery of the FOV, the spatial resolution was not greater than 2 mm within 30 mm off-center positions.

Figure 13 shows the sensitivity profile measured with various energy window settings. The maximum sensitivity values obtained at the central plane were 3.61%, 2.31% and 0.95% for the energy windows of 250–750, 350–650 and 400–600 keV, respectively.

This scanner gave the [ $^{18}\text{F}$ ]FDG PET image of a rat brain shown in the right column of figure 14. Using 3D registration software (Lee *et al* 2005), the PET image was coregistered to a CT image (figure 14, left) that was acquired immediately after the PET scan. The result is shown at the center of figure 14.



**Figure 8.** Intrinsic uniformity map of an H8500 MA-PMT.



**Figure 9.** Detector characteristics before gain compensation: (a) flood image, (b) maps of the photopeak position, (c) peak-aligned energy spectrum, (d) maps of energy resolution measured with the detector block using a PMT shown in figure 7.

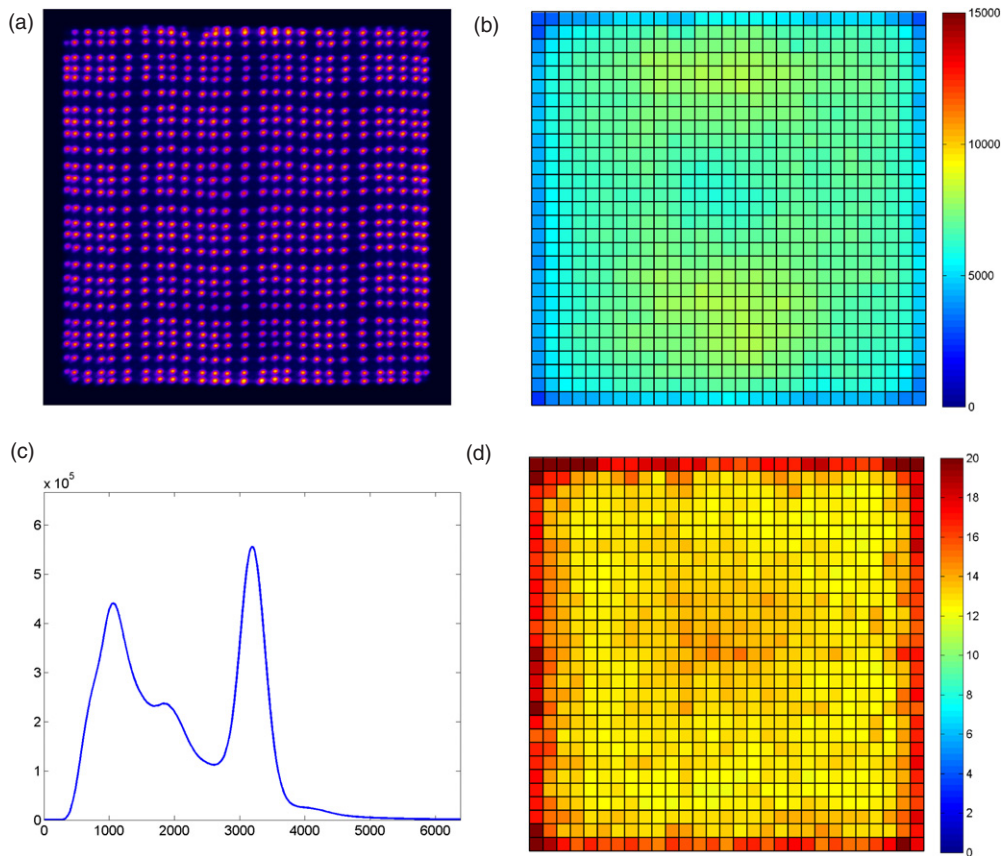


**Figure 10.** Detector characteristics after gain compensation. (a) flood image, (b) maps of the photopeak position, (c) peak-aligned energy spectrum, (d) maps of energy resolution measured with the detector block using a PMT shown in figure 7.

#### 4. Discussion

The position-sensitive MA-PMT is one of the most commonly used components in the development of NM imaging devices for small animals or specific organs. However, the degradation in the intrinsic performance of such imaging systems due to the anode gain non-uniformity of the MA-PMT is an important technical issue. Hence, there is a need for detector modules employing the position-sensitive MA-PMT to include the gain non-uniformity correction technique.

It is possible to improve the intrinsic performance of a detector module by compensating for the anode gain non-uniformity. Two different methods to do this are dominantly used. The first method uses the variable gain amplifiers (VGAs) in an application-specific integrated circuit (ASIC) (Moriya *et al* 2008). The VGAs are attached to the front-end circuit, with one VGA per channel. Moriya *et al* (2008) compared the relative photopeak position of each crystal before and after tuning the VGAs in the ASIC to provide compensation. The max/min ratio of the photopeak position improved from 3.1 to 1.9 after tuning. However, an ASIC is a

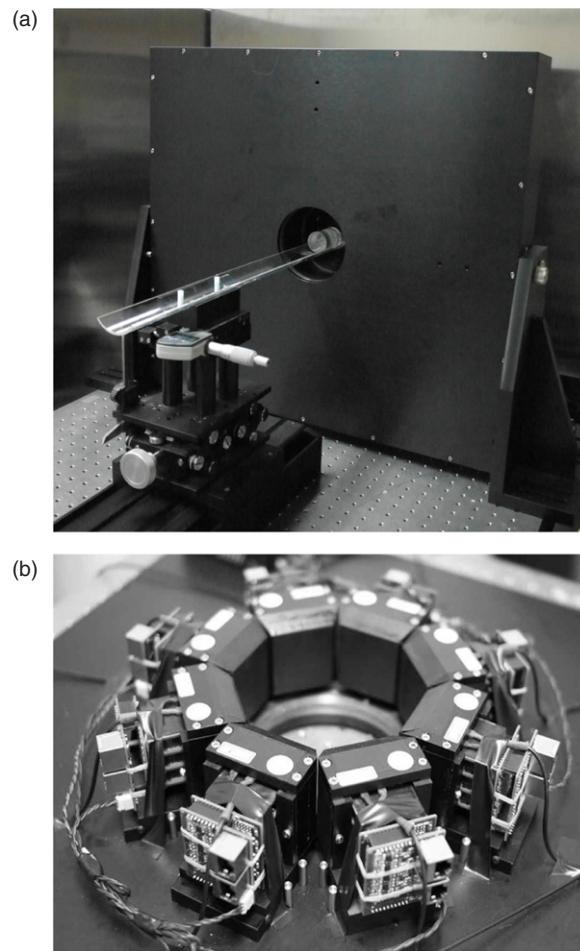


**Figure 11.** Prototype octagonal PET scanner (a) and eight detector modules with gain compensation circuits (b) assembled in the scanner.

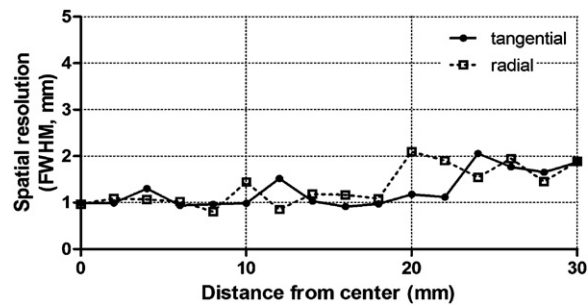


**Figure 12.** Spatial resolution versus the radial offset from the center of the scanner.

slow and expensive way to provide the compensation because of their high price and the long period needed to design and develop them.

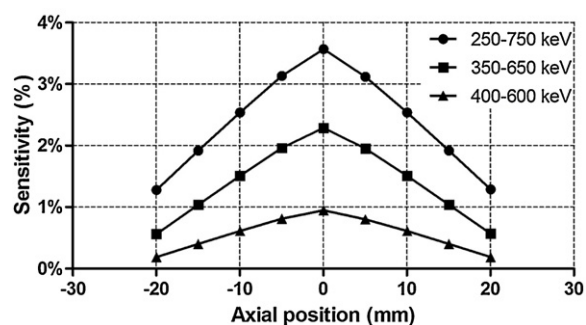


Figure 13. Sensitivity profile measured with various energy window settings.

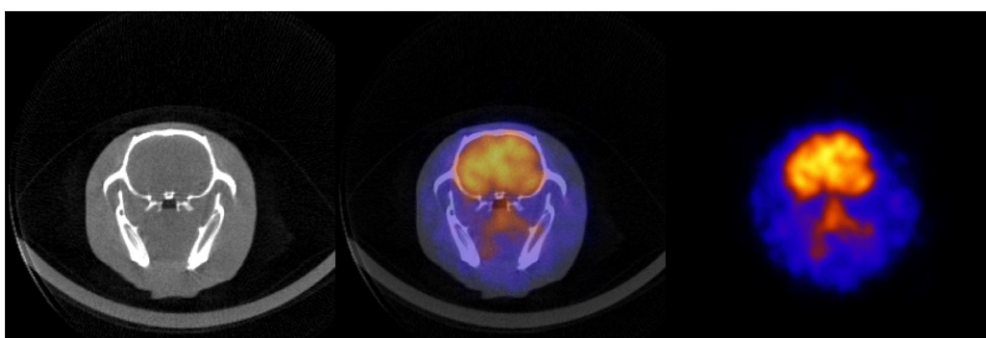


Figure 14.  $^{18}\text{F}$ FDG PET image of rat brain obtained with the prototype PET system (right), the equivalent CT image (left), and the coregistered fusion image (middle).

The other dominant method is to divide the output current from the MA-PMT anodes, as was suggested by Popov *et al* (2006a, b). This analog method is simple and inexpensive. They achieved this by adding a correction resistor to each anode. The value of the resistor was determined by a resistive matrix readout network, which decoupled each anode output into the  $X$  and  $Y$  directions to convert the 2D readout into a projective, single coordinate readout. As the authors observed, the advantage of this method is that all electronics are built from standard components. Thus, it was easily applied to a matrix readout network.

Although the approach of this paper also employs the output current division method, this method is based on an RCN circuit rather than a matrix readout network. Because the 2D RCN circuit is widely used, this new gain compensation method is useful, simple, easy to apply and inexpensive.

This work showed that our compensation method gave high-performance gain correction. Moreover, it did not take long to manufacture the gain compensation circuits, perform the iterative simulation process (two or three iterations) and implement the experimental setup. The results of the experiments presented in this paper show that the suggested method improved gain uniformity, proving its usefulness and feasibility. The system enhances the discrimination of photopeak and scatter regions in the pulse height distribution of block detectors, and can be used in the construction of high-resolution NM imaging devices.

## 5. Conclusion

A novel anode gain non-uniformity compensation method for the position-sensitive MA-PMT has been developed for application to high-performance NM imaging systems. The method described and tested in this paper will be useful for small FOV gamma cameras, SPECT and PET scanners that use position-sensitive MA-PMT.

## Acknowledgments

This work was supported by grants from the Atomic Energy R&D Program (2008-2003852, 2010-0026012) and the WCU Program (R32-10142) through the KOSEF, which is funded by the Korean Ministry of Education, Science and Technology.

## References

- Alva-Sanchez H, Murrieta T, Moreno-Barbosa E, Brandan M E, Ruiz-Trejo C, Martinez-Davalos A and Rodriguez-Villafuerte M 2010 A small-animal PET system based on LYSO crystal arrays, PS-PMTs and a PCI DAQ board *IEEE Trans. Nucl. Sci.* **57** 85–93
- Hong S J, Kwon S I, Ito M, Lee G S, Sim K S, Park K S, Rhee J T and Lee J S 2008 Concept verification of three-layer DOI detectors for small animal PET *IEEE Trans. Nucl. Sci.* **55** 912–7
- Ito M, Lee J S, Kwon S I, Lee G S, Hong B, Lee K S, Sim K S, Lee S J, Rhee J T and Hong S J 2010a A four-layer DOI detector with a relative offset for use in an animal PET system *IEEE Trans. Nucl. Sci.* **57** 976–81
- Ito M, Lee J S, Park M J, Sim K S and Hong S J 2010b Design and simulation of a novel method for determining depth-of-interaction in a PET scintillation crystal array using a single-ended readout by a multi-anode PMT *Phys. Med. Biol.* **55** 3827–41
- Kim J S, Lee J S, Im K C, Kim S J, Kim S Y, Lee D S and Moon D H 2007 Performance measurement of the microPET focus 120 scanner *J. Nucl. Med.* **48** 1527–35
- Ko G B, Yoon H S, Kwon S I, Hong S J, Lee D S and Lee J S 2011 Development of FPGA-based coincidence units with veto function *Biomed. Eng. Lett.* **1** 27–31
- Kwon S I, Hong S J, Ito M, Yoon H S, Lee G S, Sim K S, Rhee J T, Lee D S and Lee J S 2008 Development of position encoding circuit for a multi-anode position sensitive photomultiplier tube *Nucl. Med. Mol. Imaging* **42** 269–477
- Kwon S I *et al* 2011 Development of small-animal PET prototype using silicon photomultiplier (SiPM): initial results of phantom and animal imaging studies *J. Nucl. Med.* **52** 572–9
- Lee J S 2010 Technical advances in current PET and hybrid imaging systems *Open Nucl. Med. J.* **2** 192–208
- Lee J S, Park K S, Lee D S, Lee C W, Chung J K and Lee M C 2005 Development and applications of a software for functional image registration (FIRE) *Comput. Methods Programs Biomed.* **78** 157–64
- Lee M, Lee Y, Hwang K H, Choe W and Park C Y 2011 Usefulness of F-18 FDG PET/CT in assessment of recurrence of cervical cancer after treatment *Nucl. Med. Mol. Imaging* **45** 111–6
- Loudos G, Majewski S, Wojcik R, Weisenberger A, Sakellios N, Nikita K, Uzunoglu N, Bouziotis P, Xanthopoulos S and Varvarigou A 2007 Performance evaluation of a dedicated camera suitable for dynamic radiopharmaceuticals evaluation in small animals *IEEE Trans. Nucl. Sci.* **54** 454–60
- More M J, Goodale P J, Majewski S and Williams M B 2006 Evaluation of gamma cameras for use in dedicated breast imaging *IEEE Trans. Nucl. Sci.* **53** 2675–9
- Moriya T, Omura T, Watanabe M and Yamashita T 2008 Development of a position-sensitive detector for TOF-PET *IEEE Trans. Nucl. Sci.* **55** 2455–9
- National Electrical Manufacturers Association 2008 Performance measurements of small animal positron emission tomographs *NEMA Standards Publication NU 4-2008* (Rosslyn, VA: National Electrical Manufacturers Association)
- Olcott P D, Talcott J A, Levin C S, Habte F and Foudray A M K 2005 Compact readout electronics for position sensitive photomultiplier tubes *IEEE Trans. Nucl. Sci.* **52** 21–7
- Pani R *et al* 2007 Factors affecting Hamamatsu H8500 flat panel PMT calibration for gamma ray imaging *IEEE Trans. Nucl. Sci.* **54** 438–43
- Pichler B J, Wehr H F and Judenhofer M S 2008 Latest advances in molecular imaging instrumentation *J. Nucl. Med.* **49** 5S–23S

- Popov V and Majewski S 2006 A compact high performance readout electronics solution for H9500 Hamamatsu 256 multianode photomultiplier tube for application in gamma cameras *IEEE Nucl. Sci. Symp. Med. Imaging. Conf. Record* p 2981
- Popov V, Majewski S and Welch B L 2006 A novel readout concept for multianode photomultiplier tubes with pad matrix anode layout *Nucl. Instrum. Methods A* **567** 319–22
- Raylman R R *et al* 2008 The positron emission mammography/tomography breast imaging and biopsy system (PEM/PET): design, construction and phantom-based measurements *Phys. Med. Biol.* **53** 637–53
- Rouze N C, Schmand M, Siegel S and Hutchins G D 2004 Design of a small animal PET imaging system with 1 microliter volume resolution *IEEE Trans. Nucl. Sci.* **51** 757–63
- Siegel S, Silverman R W, Shao Y P and Cherry S R 1996 Simple charge division readouts for imaging scintillator arrays using a multi-channel PMT *IEEE Trans. Nucl. Sci.* **43** 1634–41
- Zhu A and Shim H 2011 Current molecular imaging positron emitting radiotracers in oncology *Nucl. Med. Mol. Imaging* **45** 1–14